Final Report to the
National Science Foundation (NSF)

Functional Integrated Phononic Crystal Structures for Wireless Applications

Georgia Institute of Technology

Principal Investigator:

Ali Adibi

Professor
School of Electrical and Computer Engineering
Georgia Institute of Technology
Atlanta, GA 30332-0250
e-mail:adibi@ee.gatech.edu
Tel: (404) 385-2738
Fax: (404) 894-4641

I. Introduction

This progress report summarizes achievements in Dr. Adibi's research group at Georgia Institute of Technology in the area of phononic crystals (PnCs) supported by National Science Foundation for the period between May 2009 to August 2012. Only major achievements with brief descriptions are listed in this report. Detailed information can directly be requested from Dr. Adibi.

This NSF-supported research has started in May 2009 and is directed toward realizing and characterizing two-dimensional (2D) periodic structures with embedded acoustic wave scatterers in a background solid slab for integrable acoustic wave devices for communications applications. To achieve this goal, as was suggested in our original proposal, our approach can be summarized in the following four categories:

1) Development of high performance fundamental PnC devices (cavities and waveguides)
2) Development of functional PnC slab devices based on the PnC slabs cavities and waveguides
3) Development of optimized fabrication processes for PnC structures
4) Characterization of PnC devices

In what follows, we conclude our main accomplishments in the above mentioned divisions in this year and the prior years as this is the final report in this series, address facing challenges, and suggest future work to overcome these challenges to implement the functionalities of phononic crystals in wireless communication systems.

II. Research Accomplishments

II.A Development of High Performance Fundamental PnC Devices

Micromechanical (MM) resonators operating at high frequencies are of great interest in the area of communications and sensing due to their unique characteristics (such as high quality factors (Qs)) that are not obtainable using electronic components. Especially, MM structures that can be fabricated on the same chip with electronic circuits are desired as they can lead to integrated and miniaturized devices for the demanding market of communications and sensing systems. High-Q MM resonators, along with waveguides, are the heart and the main building blocks of several types of MM systems that are widely used in wireless communication and sensing systems. Often a higher Q can provide a better performance for each of these devices; for instance, a resonator with higher Q can lead to radio frequency filters with sharper transition bands and lower insertion loss and sensors with better sensitivity. We summarize the main achievements in this area including the design, fabrication, and characterization of a support loss free resonator, development of an efficient phononic crystal waveguide, and a waveguide-based resonator, development of the fabrication process for AlN-based PnC devices, and development of PnC structures using silicon plate with metallic pillars.

II.A.1. Support Loss Free PnC MM Resonators

A MM Resonator with Supports

To obtain the possibility of suppressing support loss in MM resonators, we designed a typical two-port MM resonator. Figure 1(a) shows the layout of this MM resonator which shows the device layer etched regions, the supporting structures, the two metallic electrodes and the backside release etch regions. The width of the supporting structures are chosen small enough to reduce the loss. The dimension of the device is chosen so that the first order resonant modes in the *x* direction falls in the 100-120 MHz frequency range. The dimension in the *y* direction is chosen large compared to the support structures to increase the Q and also to reduce the insertion loss. Figure 1(b) shows a cross section of the structure cut normal to the *y* direction. The released 15µm Si device layer, the ~1µm ZnO layer and the 100 nm lower gold and upper aluminum (Al) electrodes are shown in Fig. 1(b).

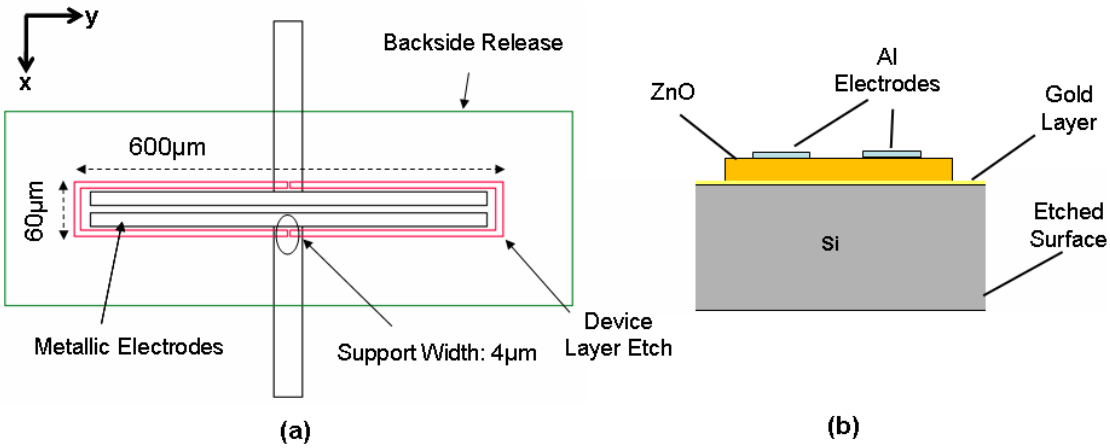

Figure 1. (a) Layout of the designed MM resonator with 4 µm supporting structures (b) cross section of the designed MM resonator with Si device layer, the ~1µm ZnO layer and the 100 nm lower gold and upper Al electrodes

To characterize the performance of this MM resonator, we fabricated the structure using a CMOS compatible fabrication process. We start with a Si on insulator (SOI) wafer with a device layer of 15 µm, buried oxide layer of 2 µm, and a 400 µm handle layer. The main resonant structure is formed first by etching the device layer of the SOI wafer using inductively couple plasma (ICP). Then, in order to fabricate the thin transducer stack, a 100 nm layer of gold is deposited on top of the PnC cavity structure to form the first electrode of the transducer. Approximately 1 µm of piezoelectric ZnO is sputtered and patterned on the resonant region with its *c*-axis aligned to the *z* direction. Finally, a 100 nm Al electrode is patterned using a lift off process to complete the transducer fabrication. The top Al electrode and the ZnO regions uniformly cover the whole resonator length in the *y* direction. The long cavity region provides enough transduction area to better couple electrical energy into the acoustic modes of the resonator.

A top-view scanning electron microscope (SEM) image of the fabricated structure is shown in Figure 2(a). In order to de-couple the PnC slab from the substrate, the SOI wafer is patterned on the back using optical lithography and deep plasma etching.

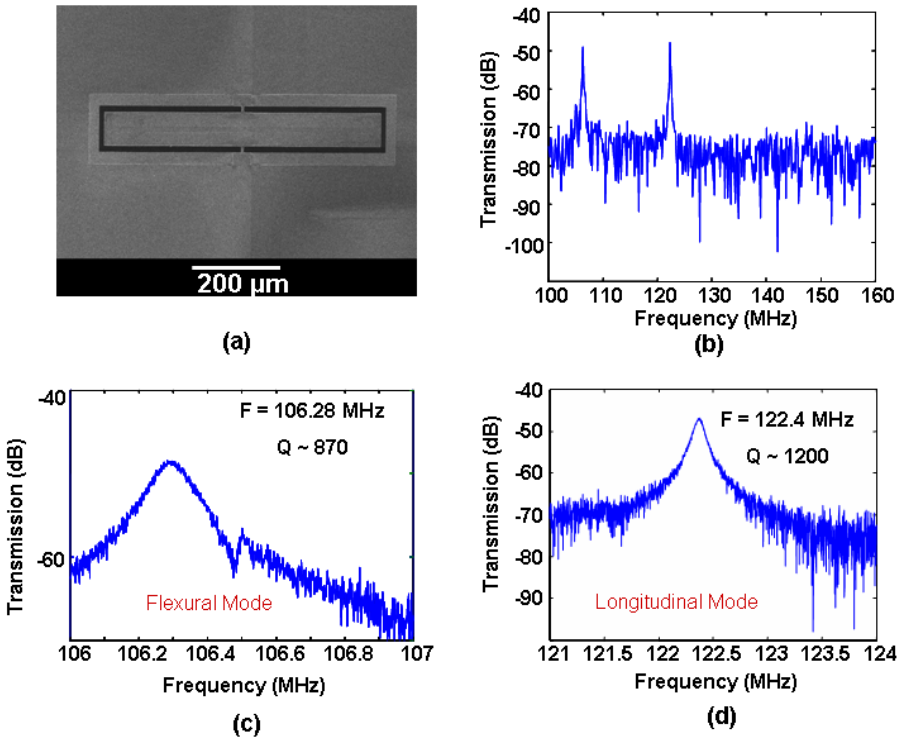

Figure 2. (a) Scanning electron microscope (SEM) image of the designed conventional MM resonator (b) the transmission spectrum between the two ports of the resonator in the range of interest (c) high-resolution characteristics of the flexural resonant mode (d) high-resolution characteristics of the longitudinal mode

To characterize this structure, we used a vector network analyzer and measured the transmission profile of the resonator in the range of interest, i.e., 100 MHz to 160 MHz. Figure 3(b) shows the transmission profile of the device where two resonant peaks appear in the transmission spectrum at ~106.3, and 122.4 MHz. Finite element simulations show that these two modes are associated with a flexural and a longitudinal (extensional) vibration mode, respectively. To obtain the Qs of these two modes, higher frequency resolutions of these modes are also measured and Qs of 870 and 1,200 are obtained for the flexural and longitudinal modes, respectively. The Qs are obtained by measuring the full width at half maximum of the resonant peaks in the spectrum.

Design of a Support Loss-free PnC Resonator

To characterize the role of the supporting structures in determining the Q of the resonator, we also fabricated a similar resonant structure but with PnC structures to provide the mechanical support. The layout of the designed PnC resonator is shown in Figure 3.

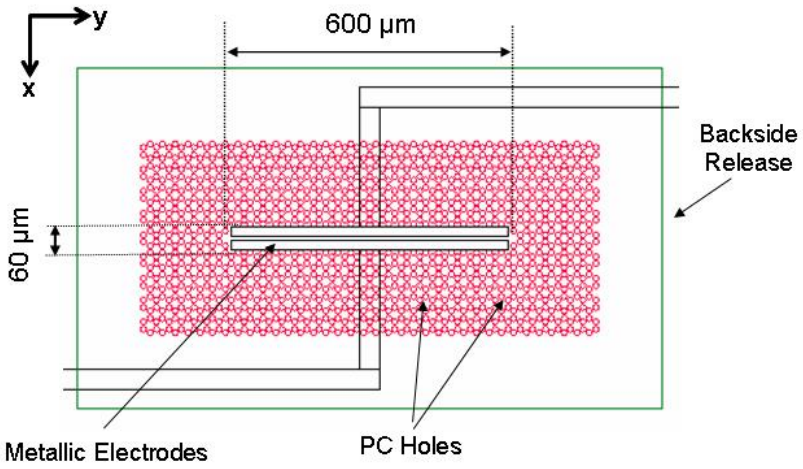

Figure 3. Layout of a virtually support loss-free PnC resonator

The designed PnC structure in this figure, is made of a hexagonal (honeycomb) array of circular inclusions with radius of r = 6.4 µm, and the distance between the centers of the two nearest holes of a= 15 µm. With a thickness of d =15 µm, this structure would show a large complete PnBG of 117 MHz < $f \times a$ < 151 MHz, with f being the acoustic frequency. The line defect is created by eliminating one period (4 rows) of holes in the x (ΓK direction of the PnC) direction as shown in Figure 3. The distance between the centers of the nearest holes in the x and y directions across the cavity is 60 µm and 600 µm, respectively. This complies with the structure of the conventional MM resonator reported in the previous section to perform a relative comparison.

This PnC resonator configuration and its fabrication process have several merits. The possibility of fabrication with standard MM fabrication technologies and post-CMOS fabrication compatibility enables inexpensive manufacturing and integration with electronic circuits. Fabrication of the structure in SCS also enables the use of superb mechanical properties of SCS including its low loss in the frequency range of interest. The possibility of engineering the structure in two dimensions provides ample flexibility in the design of the PnC resonator. Further, the possibility of making more compact structures (e.g., 2D point-defect PnC resonators) as compared to the one-dimensional resonator structures adds another advantage. Direct excitation of the resonant modes by fabricating the transducer on top of the resonant region enables the realization of more compact devices. This is due to the fact that the high Q of the resonator leads to a reduced level of motional impedance and insertion loss compared to the large number of IDTs needed for resonant tunneling excitation. Also, with direct excitation, the number of PnC periods placed around the resonant region can be increased to provide enough isolation from the surroundings. This can eliminate the reduction in the Q due to the support (coupling) loss to the surroundings as compared to the resonant tunneling excitation method.

Figure 4(a) shows an SEM image of the fabricated PnC resonator. The transmission profile of the modes propagating from one port to the other are shown in Figure 4(b) and 4(c) for the flexural and longitudinal vibrations, respectively. As it can be seen, the resonant modes show an increased Q of approximately 6,000 which is approximately six times the Q of the modes of the fabricated conventional MM resonator. However, as it can be seen in this figure, multiple resonant modes are supported by the structure in each frequency region. This is mainly because of the different standing vibration modes with different lobes in the y direction within the cavity.

This kind of behavior is not observed in the conventional MM resonator since the reflectors are not corrugated as for the case of the PnC resonator. As such multiple modes are not usually desirable for communications and sensing applications, different methods are under investigation to effectively suppress such spurious modes.

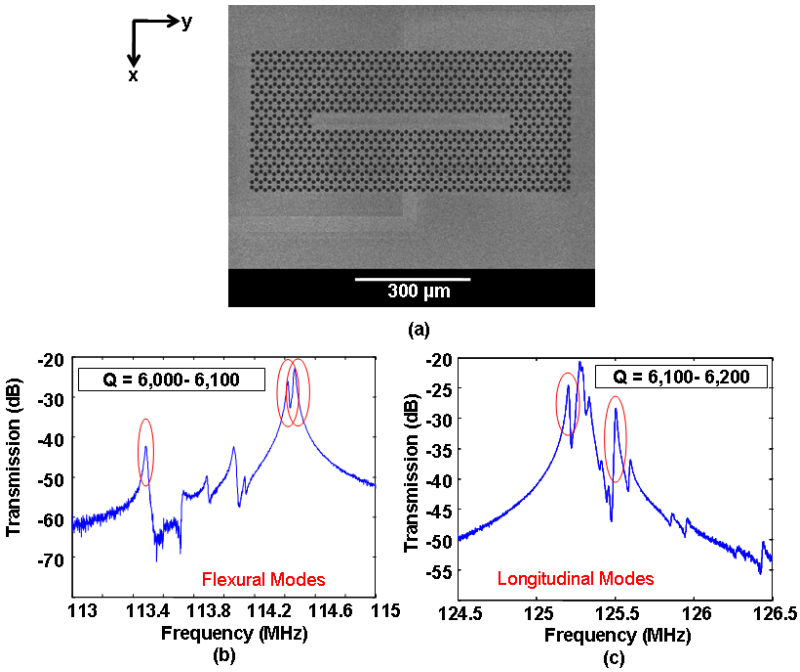

Figure 4. (a) SEM image of the fabricated PnC-surrounded resonator structure (b) first-order flexural resonant modes of the structure in the x direction; multiple modes are excited because of the PnC structure (c) first-order longitudinal (extensional) modes present in the PnC structure

II.A.2. Development of an Efficient Phononic Crystal Waveguide

To eliminate the problem of spurious modes, we propose to implement a PnC waveguide with limited number of supported modes. The PnC waveguide then can be confined by the PnC structure on its input and output so that it can confine forward and backward (and hence standing) waves within the waveguide region.

The PnC structure is composed of a hexagonal (honeycomb) lattice of void holes in a free-standing Si slab. If the thickness of the slab is represented by a, the lattice constant and the radius of the holes are a and $0.43a$, respectively. As previously reported, the extent of the CPnBG for such a geometry is 1750 m/s $< f \times a <$ 2265 m/s. Although we have previously shown the possibility of waveguiding in the PnC structures [1], the waveguides reported so far support many modes within the CPnBG. Such multi-mode nature of the developed waveguides limits their application and the usable bandwidth. Therefore, a PnC waveguide with reduced number of modes is introduced. In order to obtain such a waveguide, instead of removing lines of holes completely, PnC holes in two rows are reduced in size to form a waveguide. A schematic of such PnC waveguide is shown in Figure 5.

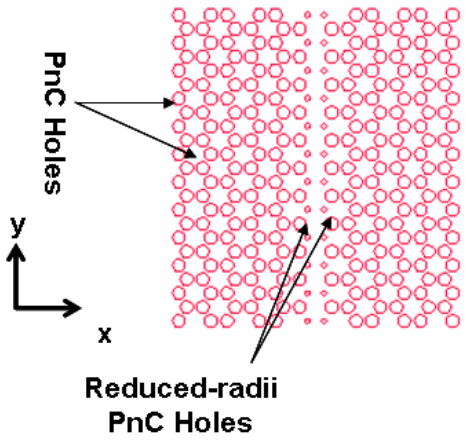

Figure 5. Layout of the designed phononic crystal waveguide. Two rows of holes in the PnC structure are reduced in size to allow for a limited number of guided modes in the formed PnC waveguide.

The dispersion profile of the waveguide shown in Figure 1 for the reduced PnC holes with radius of 0.2*a* is given in Figure 6. By considering the profiles of each mode in the wave vector domain (e.g., at Γ and K points), the size of the holes is chosen based on the dispersion curve characteristics and the profile of the propagating modes in the formed waveguide.

Waveguide-based PnC Resonator

In order to form the PnC resonator based on the PnC waveguide, the input and output ports of the waveguide are blocked by the PnC structure. The length of the confined waveguide is ten periods. This leads to the formation of an efficient waveguide-based PnC resonator. In order to interrogate the resonator, a 100 nm gold layer is deposited on top of the resonator to form as a common excitation/detection electrode. A 1 μm layer of piezoelectric zinc-oxide is sputtered on top of the gold layer to serve as the transduction medium. A 100 nm aluminum (Al) layer is then patterned on top of the structure to form the second excitation/detection electrode to interrogate the appropriate resonant modes.

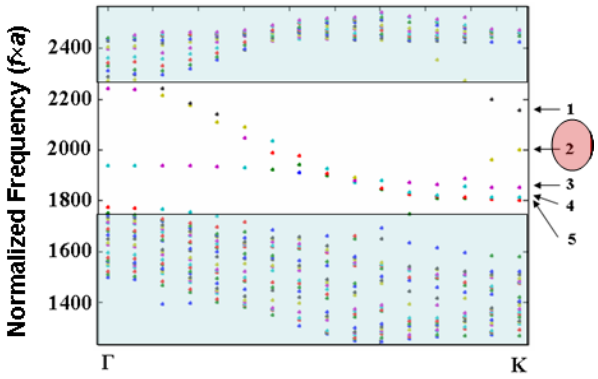

Figure 6. The dispersion characteristics of the PnC waveguide shown in *Error! Reference source not found.*. ***As indicated in this figure, five modes appear in the dispersion profile of the waveguide within the CPnBG of the PnC***

A Schematic of the layout, and a scanning electron microscope (SEM) image of the fabricated structure are shown in Figures 7 and 8, respectively.

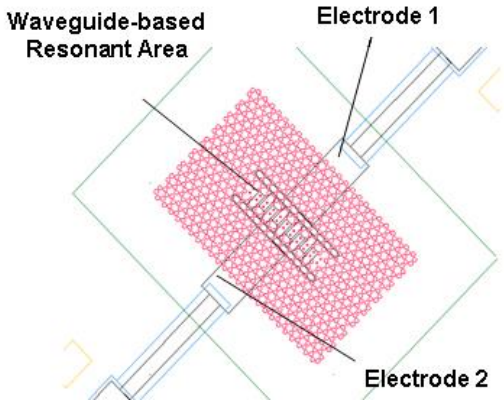

Figure 7. Schematic of the layout of a waveguide-based PnC slab resonator structure.

The Al electrodes are placed on top of the resonant region to effectively excite the mode of interest, which is an extensional mode indicated by number 2 in Figure 6.

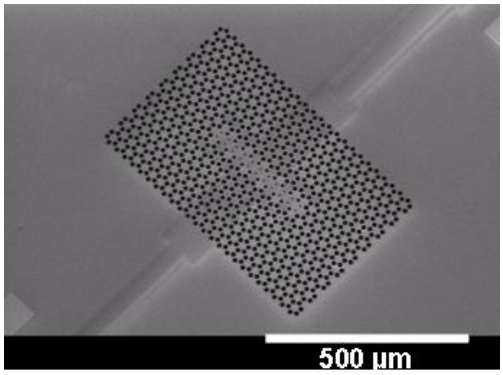

Figure 8. SEM image of the fabricated waveguide-based MM PnC resonator.

In order to accurately evaluate the resonance properties of the excited mode, we fit a Butterworth Van Dyke model [2] to the resonant profile of the structure measured through a vector network analyzer. The resonance profile of the fabricated waveguide-based MM PnC resonator in the form of admittance is shown in Figure 9. The resonance parameters extracted from fitting a BVD model are also given in the graph, where f, Q, R_m, C_p, and R_p represent the frequency of resonance, the quality factor, the motional impedance, the parallel capacitance, and the parallel resistance, respectively.

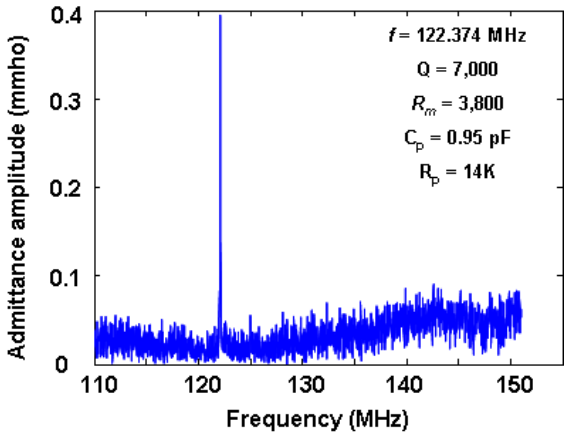

Figure 9. Admittance profile of the waveguide-based PnC resonator.

As can be seen in this figure, the Q of the resonance is 7,000 which is slightly higher than the previously reported PnC resonators fabricated on the same chip and went through an exact same fabrication process [3] confirming the suppression of the support loss. The frequency of resonance of the MM resonator is 122.374 MHz, which is about % 9 lower than what predicted through the simulations. The reason can be clearly attributed to the transducer stack placed on top of the Si slab, which reduces the propagation phase velocity of the waves. The effect of this stack is not included in the simulations. It is worth noting that the resonance profile is free of any spurious modes, which offers a very large spurious-free spectral range. This shows that obtaining support-loss free MM resonators is possible through the use of PnC structures. Although the mechanism of excitation is based on piezoelectric transducers (which limits the achievable Q due to the transducer material loss), this method of obtaining support loss-free resonators can be extended to MM resonators with other means of excitation.

II.B Development of Optimized Fabrication Processe for PnC Structures

AlN-based piezoelectric excitation of PnC structures

As AlN is a more CMOS compatible material compared to ZnO (Zn is not compatible for CMOS) and provides better coupling and quality factors as a piezoelectric excitation medium, we developed an efficient fabrication process for fabricating our PnC structures.

As an example, the waveguide-based resonator structure is also fabricated with the scaling choice of a = d = 15 µm for the PnC structure using a post-CMOS compatible fabrication process based on AlN piezoelectric excitation.

The schematics of different fabrication steps in the developed process are shown in Figure 10. The process starts with a high-resistivity (to reduce electromagnetic coupling) silicon on insulator (SOI) wafer with a 15µm device layer, a 2µm buried oxide (BOX) layer and a 400µm handle layer) [Figure 10(a)]. A 100nm/1µm/100nm stack of Mo/AlN/Mo is sputtered on top of the device layer (this step was performed at Tegal Co.) [Figure 10(b)]. The top Mo layer is patterned first using optical lithography and plasma etching to form the top electrode and contact pads [Figure 10(c)]. PnC holes are etched using a two-step plasma etching recipe to etch the transducer stack and the Si device layer [Figure 10(d)]. The access to the lower Mo electrode is obtained by selective wet etching of the AlN layer over the Mo layer [Figure 10(e)]. Finally, the

structure is etched from the back using backside-alignment lithography and deep plasma etching of the handle and the BOX layers to release the structure and form the PnC slab resonator [Figure 10(f)].

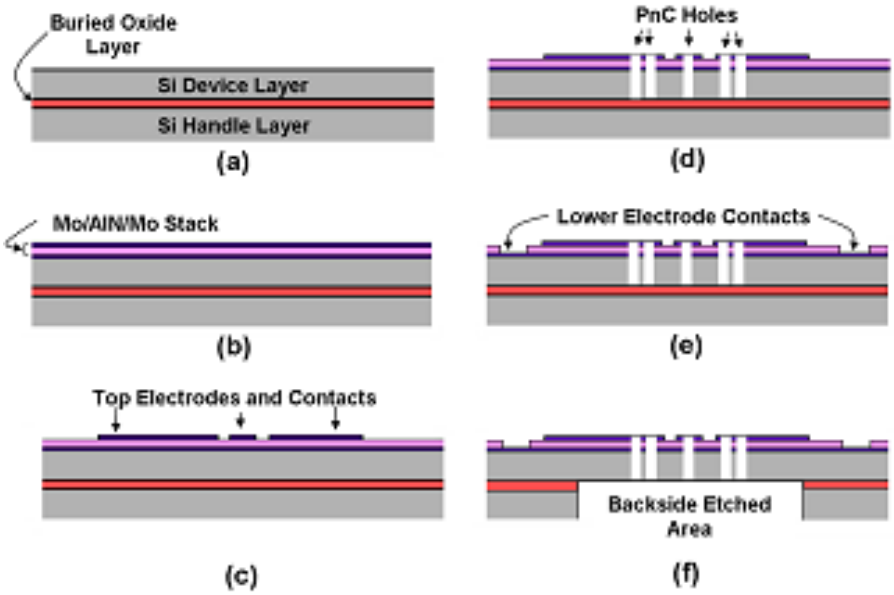

Figure 10. Fabrication steps for PnC waveguide-based resonators. The fabrication process starts with (a) an SOI wafer. (b) A stack of Mo/AlN/Mo is sputtered on top of the wafer. (c) The top Mo electrode is patterned. (d) PnC holes are then etched using dry etching. (e) AlN layer is removed from selected locations to provide contact port to the PnC structure. (f) The structure is etched from the backside using deep plasma etching to remove the handle Si and the BOX layers to release the PnC slab structure at the desired locations.

A top view scanning electron microscope (SEM) image of the fabricated structure is shown in Figure 8. The approximate geometrical parameters of the fabricated PnC resonator are measured to be a = 15 µm, 2r = 12.5 µm (r ~ 0.42a), and 2r'= 4.9 µm (r'~ 0.16a) using the SEM data. As noted, the values for the fabricated results are slightly smaller than the designed values due to fabrication imperfections. This can be fixed by compensating the designated sizes in the mask layers to correct for such fabrication imperfections.

The structure is characterized using a two-port vector network analyzer with 50Ω reference impedance to obtain the scattering parameters of the device in the CPnBG frequency range. The main excited mode of the structure is located at f = 134.14 MHz, and its transmission and reflection parameters are considerably dominant over other modes of the resonator.

In order to accurately evaluate the resonance properties of the main excited mode, we fitted a modified Butterworth Van Dyke (BVD) model to the admittance profile of the selected mode. The Q of the resonance is 13,500, which is by far the highest Q reported for PnC resonators and significantly higher (>30 %) than the results reported using the most advanced techniques for resonators with a similar structure (AlN stack on 15 µm Si) measured in air, confirming the suppression of the support loss. The frequency of resonance of the MM resonator is 134.1418 MHz, which translates to the normalized frequency of f × a = 2012. Besides the high Q of the resonance, the spurious-free range of the resonance is also worth noting. The resonance is more than 10 MHz apart from any resonance within 35 dB of its power, which gives a large frequency

range of operation. This result confirms that obtaining high quality support-loss free MM resonators is possible through the use of the PnC structures. Although the mechanism of excitation is based on piezoelectric transducers in this paper (which limits the maximum achievable Q due to the transducer material loss), this method of obtaining support loss-free resonators can be extended to MM resonators with other means of excitation.

These results show the advantages of AlN-based excitation over our previous technology using ZnO.

II.C Development of Phononic Crystal Structures using Silicon Plate with Metallic Pillars

Different approaches have been proposed in order to realize PnCs including complete three-dimensional (3D) arrangement of inclusions in a host material [4], surface acoustic wave (SAW) -based PnCs [5], and inclusions or air holes in a two-dimensional (2D) plate [6,7]. The fabrication of 3D structures for high frequency applications is challenging due to the shrinking feature sizes and the loss of mechanical energy in the SAW-based devices through coupling to the bulk modes makes this architecture less desirable [5]. As a result, the 2D plate-based (or membrane-based) PnCs have attracted a lot of attention. The advantage of the Si-based PnC plates include: 1) possessing complete PnBG and providing 3D confinement of the acoustic energy, and 2) ease of fabrication using CMOS processes including photolithography and dry/wet etching. While the overall process of fabricating 2D PnC plates can be straightforward, the fabrication challenges associated with the high filling fractions encountered in the hole-based 2D PnCs can hinder the fabrication process [7]. To avoid the use of hole-based PnCs, an alternative PnC architecture based on the use of a periodic array of metallic (e.g. aluminium) stubs on a proper plate (e.g. aluminium) have been proposed [8,9] and experimentally demonstrated [8]. Such stub-based (or pillar-based) structures provide PnBG without stringent etching requirements [8]. The schematic of the pillar-based PnCs is shown in Figure 11(left). This structure provides another degree of freedom in designing the PnC, i.e. the height of the pillars (h), in addition to the radius of the pillars (r), the slab thickness (d), and the lattice period (a); the geometrical design parameters which are already considered in the conventional (hole-based) 2D PnCs. Based on the finite element simulation, we have concluded that one can manipulate the center frequency of the PnBG by adjusting the height of pillars. This property is specific to the pillar-based structures as the PnBG center frequency of a hole-based structure is determined by only its holes radius and the slab thickness.

Having the ability to fine-tune the center frequency of the PnBG using pillar-based PnC structures was part of our focus. We investigated an array of metallic pillars on a slab of silicon (Si). We have chosen the pillar-based structure for our investigation because of the relaxed fabrication requirements for this type of structure as well as the extended flexibility in designing the PnCs using this structure as supported by our finite-element calculations.

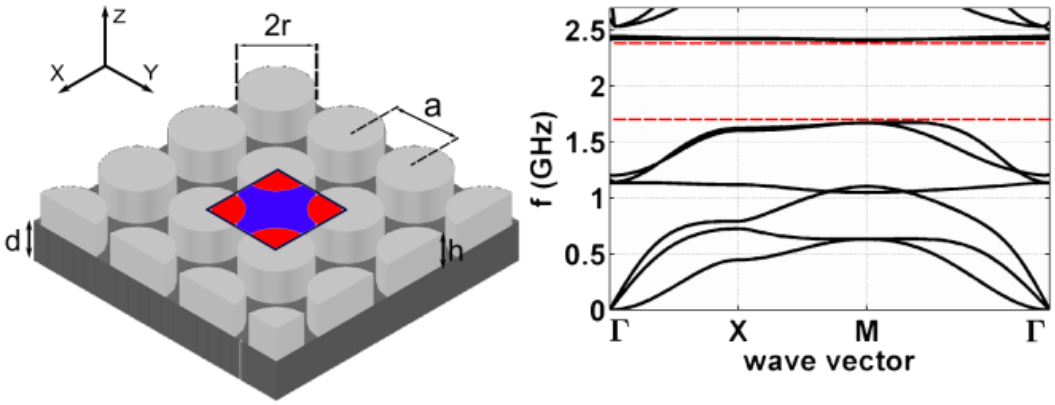

Figure 11. (left) Structure and unit cell of the pillar-based PnC with square lattice and (right) its band diagram for a = 1μm, d = 0.5μm, r = 0.4μm and h = 0.4μm.

In what follows, existence of PnBGs is shown in a PnC structure composed of a silicon plate with stubbed tungsten pillars. Using the finite element method for numerical simulations, the evolution of band gap opening with varying design parameters is studied. Several band gaps have been observed for different lattice symmetries. It has been shown that PnBGs of up to 40% gap to mid-gap ratio can be achieved for the triangular and square lattice. We will present a summary of our work in devising a systematic theoretical study of the PnC structure composed of an array of cylindrical tungsten (W) pillars deposited over a silicon plate (Figure 11(left)). We have focused on the application of Si/W material system that provides CMOS compatibility. Additionally, Si and W have good mechanical impedance mismatch, which is crucial for opening PnBG. We will show the existence of PnBG in three different symmetries (square, triangular, and honeycomb) and will discuss the effect of lattice symmetry on the formation of PnBG. It will be shown that the triangular lattice is the favorable symmetry system for the pillar-based structure to provide the widest band gaps, in contrast to the hole-based 2D PnC, which has the largest PnBG in the honeycomb lattice [7]. We will also show that introducing the 4th parameter (h) into the design space can alleviate the fabrication challenges associated with the high filling fraction observed in the previous PC designs.

The numerical method used for the calculation of the PnC band structure in our work, is based on 3D finite element method implemented in COMSOL software environment. For the purpose of this work, we have calculated the phononic band diagram for three different lattice symmetries: square (Figure 11(left)), triangular (Figure 12(left)) and honeycomb (Figure 13(left)). In all of these three structures, the underlying plate is Si and the cylindrical stubs are made of W. The direction of x, y, and z-axes are aligned with the Si crystalline axes. The values of the stiffness tensor and material density used to calculate the PnC band structure for Si are $c_{11} = 16.6 \times 10^{10}\ \mathrm{N/m^2}$, $c_{12} = 6.4 \times 10^{10}\ \mathrm{N/m^2}$, $c_{44} = 8.0 \times 10^{10}\ \mathrm{N/m^2}$, and $\rho = 2330\ (\mathrm{kg/m^3})$. The values of the material properties used for W are $c_{11} = 52.5 \times 10^{10}\ \mathrm{N/m^2}$, $c_{12} = 20.5 \times 10^{10}\ \mathrm{N/m^2}$, and $\rho = 19300\ (\mathrm{kg/m^3})$.

The results of the finite element simulations for a carefully designed set of geometrical parameters are shown in Figure 11(right), Figure 12(right), and Figure 13(right) for the square, triangular, and honeycomb lattice structures, respectively. In these figures, the lattice spacing is a=1μm, the thickness of the Si slab is d=0.5μm, and the height and the radius of W pillars are r=h=0.4μm. As seen from Figure 11(right) and Figure 12(right), for the square and the triangular lattices, a wide PnBG can be opened around f = 2GHz. The ratio of the band gap width (upper edge – lower edge) to the center frequency of the gap is around 40%. This band gap to mid-gap

ratio is sufficient for almost all practical applications including resonators and filters designed for wireless systems. Figure 13(right) shows the band structure of the PnC structure with honeycomb lattice demonstrating the existence of two narrower band gaps around f = 1.7GHz (gap to mid-gap ratio ~ 5%) and f = 2.2 GHz (gap to mid-gap ratio ~ 10%) for this lattice. Other narrow band gaps can also be seen for triangular and honeycomb lattices around 1GHz and 600MHz, respectively. Note that given the equal lattice parameter (a) and the pillar radius (r), the filling fraction for the honeycomb lattice is smaller than that of the triangular lattice.

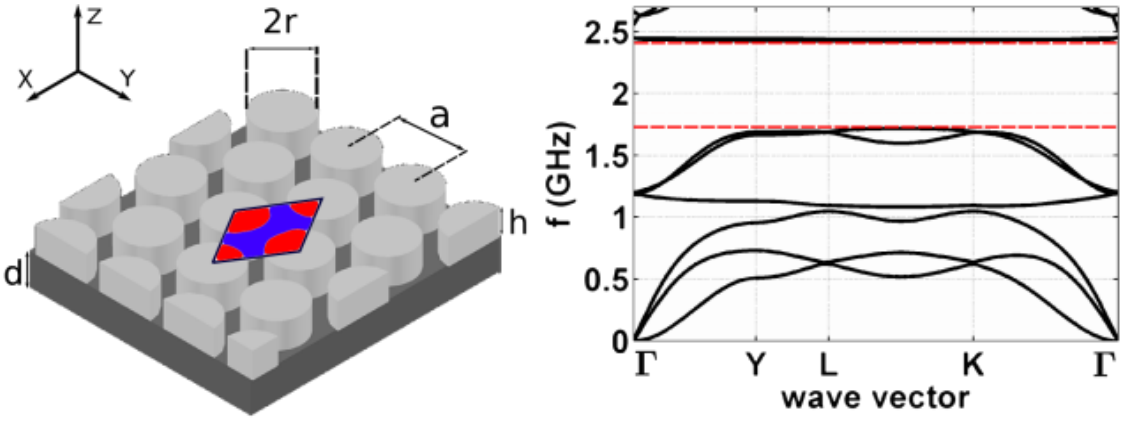

Figure 12. (left) Structure and unit cell of the pillar-based PnC with triangular lattice and (right) its band diagram for a = 1µm, d = 0.5µm, r = 0.4µm and h = 0.4µm.

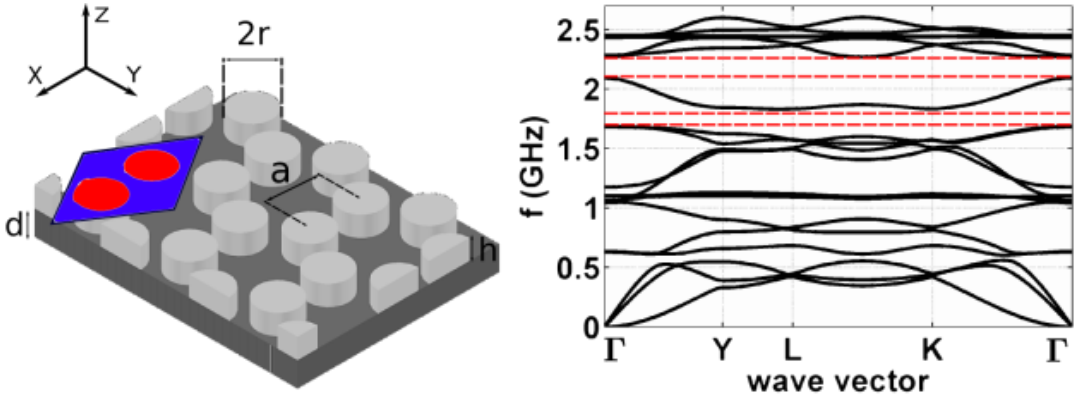

Figure 13. (left) Structure and unit cell of the pillar-based PnC with honeycomb lattice and (right) its band diagram for a = 1µm, d = 0.5µm, r = 0.4µm and h = 0.4µm.

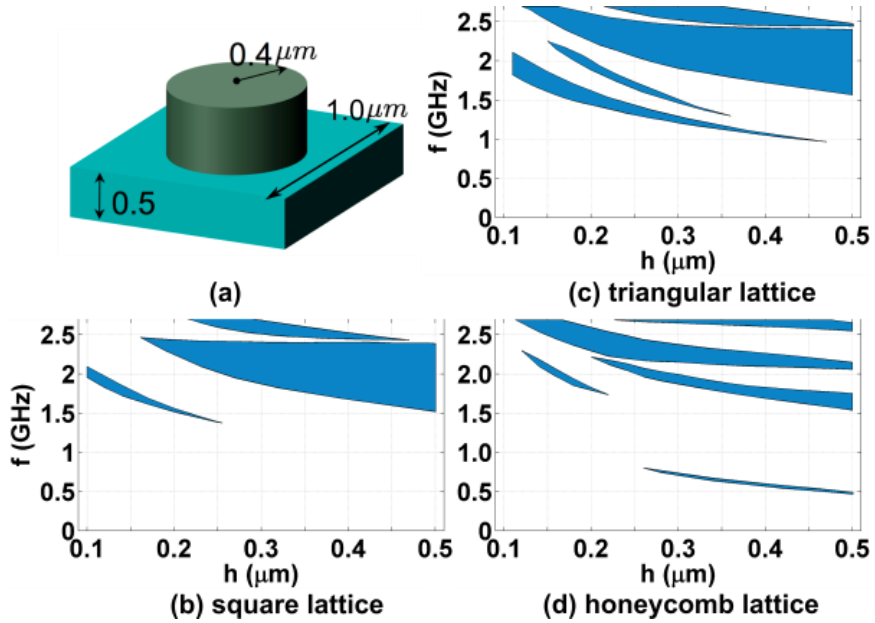

Figure 14. (a) Geometrical parameters of the PnC structure of interest. Evolution of the PnBG (gap map) for the pillar-based PnC with respect to the pillar height (h) and with geometrical parameters in a, i.e., a = 1μm, d = 0.5μm, r = 0.4μm, and h = 0.4μm, with (b) square, (c) triangular, and (d) honeycomb lattice symmetries.

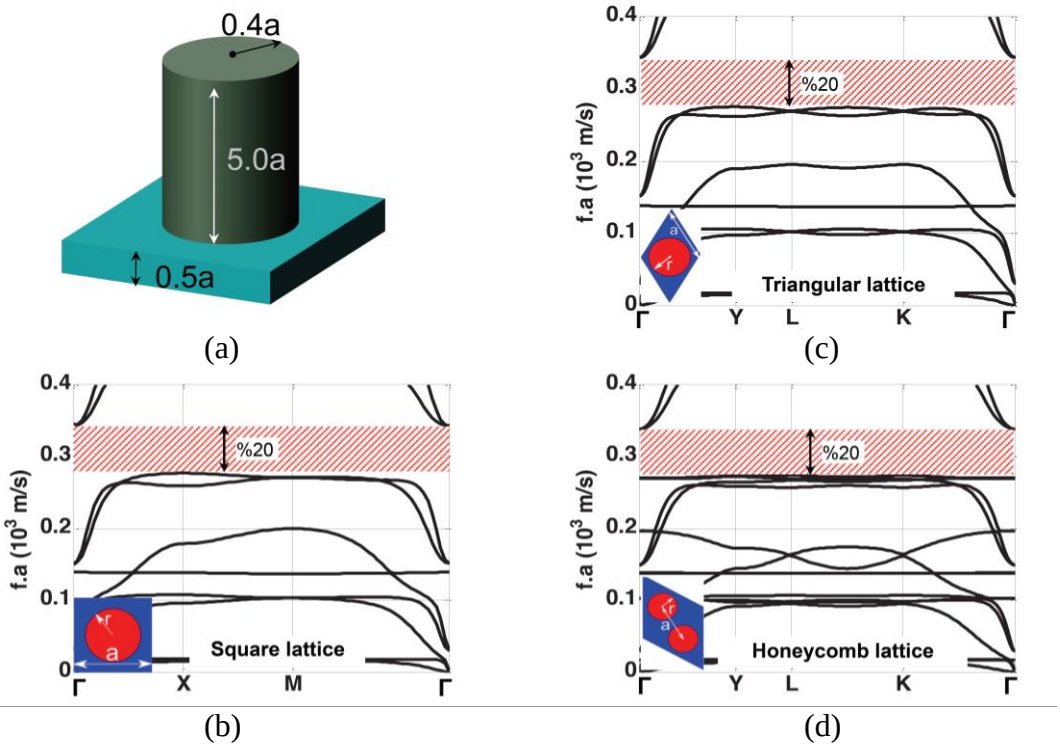

Figure 15. (a) Geometrical parameters of the PC structure of interest. Band diagram for the pillar-based PnC for tall pillars with geometrical parameters in a, i.e., a = 1μm, d = 0.5μm, r = 0.4μm, and h = 0.4μm, with (b) square, (c) triangular, and (d) honeycomb lattice symmetries.

As discussed earlier, one feature of the pillar-based PnCs is introducing the 4th geometrical parameter (h) to the design space. In order to further investigate the effect of this parameter in the opening of PnBGs, the evolution of band diagrams (aka gap map) for these 3 lattices were studied. Figure 14 shows the evolution of the PnBG openings as the height of pillars increase for the 3 lattice types with a = 1μm, d = 0.5μm, and r = 0.4μm. As seen from Figure 14, several PnBGs exist for each lattice type. It is also observed that the PBGs are generally wider for the square and triangular lattices. On the other hand, triangular and honeycomb lattice PnCs have more gaps than the square lattice in a given frequency range. These results suggest that triangular lattice outperforms the other two lattice types for the width and the number of gaps opened. From Figure 14, it is also obvious that by increasing the W pillar height (h), the center frequency of PnBGs decrease. This effect shows how this geometrical parameter can be used to accurately engineer a PnC for a desired frequency range. In order to show this property more clearly, as shown in Figure 15, one can lower the center frequency of the PnBG from around 2GHz down to 300MHz by just increasing the height of pillars from 0.4μm to 5μm.

Figure 15 shows the band structure of the pillar-based PnCs for an extreme case where the heights of the pillars are increased to five times the lattice constant (5 × a). As seen in this figure, the PnBGs in all three lattice types have identical lower and upper edges. The center frequency of these PnBGs is ≈300 m/s and the gap width (ratio of PnBG extent to its center frequency) is ≈%20.

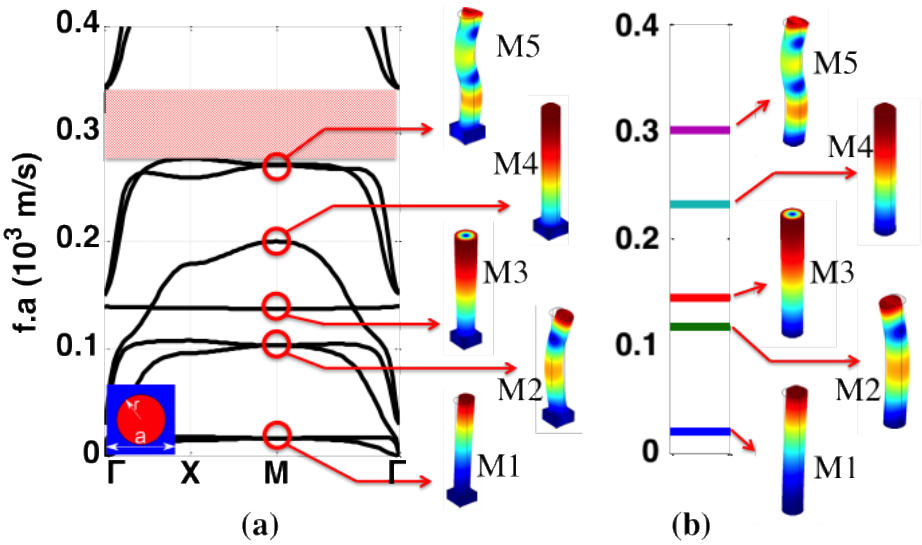

Figure 16. Comparison of the mode shapes of (a) a pillar-based PnC with W pillars arranged in a square lattice on a Si substrate with a thickness (d/a) of 0.5 at the high symmetry point of M and (b) individual pillars with fixed boundary condition at one end. The radius (r/a) and height (h/a) of pillars in both cases are 0.4 and 5.0, respectively.

The decreasing trend of the center frequency of the PnBGs with increasing pillar height and their approach to the almost identical band structure for very tall pillars suggests that the vibrational properties of the cylindrical pillars have distinguishable effect on the position and formation of the PnBGs. The decreasing trend can be attributed to the inverse relation of the resonance frequency of a rod to its length and the identical PnBGs — in case of tall pillars —

can be attributed to the dominant effect of the resonance of pillars compared to the effect of Bragg scattering and lattice periodicity.

As further evidence to the effect of pillars on the PnBGs, one can calculate the mode profile of individual pillars with the same height and radius as in the case of tall pillars (i.e., h/a = 5.0 and r/a = 0.4) and compare them with the mode profile of the unit cells for the PnCs. Figure 16(a) shows such a comparison. The displacement profiles of the first five distinct modes at high symmetry point of M in a square lattice with the same geometrical parameters as Figure 15 (i.e., h/a = 5.0, r/a = 0.4, and d/a = 0.5) are depicted as M1–M5. Figure 16(b) shows the displacement profiles of the first five distinct modes of a cylindrical pillar with identical geometrical parameters as Figure 16(a). These pillars are modeled with fixed boundary condition at one end and free boundary condition at the other end. The correspondence between the shear mode profiles (M1, M2, and M5), the breath mode profile (M3), and the longitudinal mode profile (M4) in both sides can easily be observed. These calculations show the effect of the resonance of individual pillars on determining the position of branches in the band structure of the PnC and, consequently, on the PnBGs.

Effect of Lattice Symmetry on the Position of the Bandgaps

In the previous section, we argued that the local resonance of the individual pillars could play an important role in the formation and position of the PnBGs. It was shown that this effect becomes more dominant as the height of pillars increases. To examine this argument, one can randomly perturb the position of the pillars in a super-cell and calculate the center frequency and width of the PnBG. The result of these simulations can be com- pared for pillars with different heights. As Bragg scattering and its effect on the formation of the PnBG is dependent on the lattice periodicity while the resonance of individual pillars is only dependent on the geometry of the pillars, we expect these perturbations have greater effect on the PnBGs formed through Bragg scattering — especially when the pillars are short compared to the lattice constant and the local resonance effect is not the dominant factor in the PnBG formation. As the height of pillars increases and the local resonance becomes dominant, the effect of lattice perturbation is expected to be negligible.

Figure 17(a) illustrates the displacement scheme that is used in our calculations to demonstrate the effect of lattice perturbation on the formation of PnBGs. As shown, a 3×3 super-cell is modeled with each pillar displaced following a Gaussian distribution in the x and y direction. This yields to a Chi distribution for the relative distance from the original position of each pillar (denoted as dis_{ij}) and a uniform distribution for the angle of displacement (denoted as φ_{ij}). These simulations are repeated 20 times for each chosen pillar height to model the effect of random pillar distribution and the average center frequency and width of the PnBGs are calculated, accordingly. The relative changes in the average center frequency and the PnBG width compared with the unperturbed data are shown in Figures 17(b) and (c).

As shown in Figure 17(b), for a super-cell with h/a = 0.1 the lattice perturbation with mean displacement (<dis>) of 0.05a causes an average change of %17 in the width of the PnBG. For taller pillars, this perturbation causes much smaller change (below %1) in the width of the PnBG and becomes negligible as the height of pillars increases. In comparison, for a perturbation scheme with smaller mean displacement (i.e., <dis> = 0.02a) the average change in the PnBG width is smaller but the curve follows the same trend as the larger displacement.

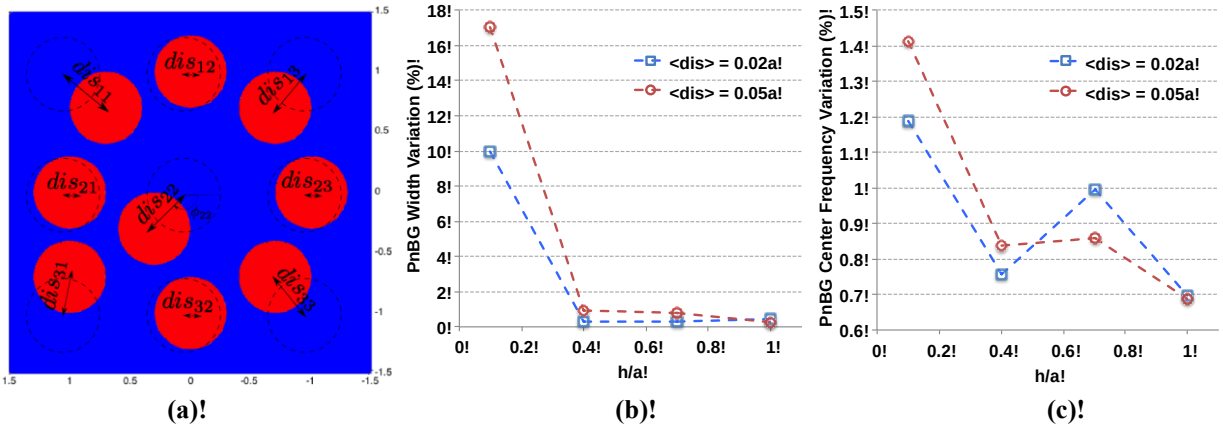

Figure 17. Effect of lattice perturbation on the width and position of the PnBGs in a 3 × 3 super-cell of W pillars and Si substrate. (a) Pillar displacement scheme used for modeling the effect of lattice perturbation on PnBGs. dis_{ij} and φ_{ij} denotes the displacement distance and angle of pillar number ij. Variation of the PnBG (b) width and (c) center frequency is shown for different pillar heights and mean displacements. The PnBG in unperturbed super-cell is used as the reference for calculating the relative changes shown in these figures.

Figure 17(c) depicts the average change in the center frequency of the PnBG for pillars of different height. It can also be seen that, in general, as the height of pillars increases, the smaller the effect of lattice perturbation becomes. One exception to this observation is when h/a = 0.7 where the average change in the center frequency of the PnBG is greater than the change for h/a = 0.4. One might attribute this result to the interaction of Bragg scattering and local resonance, insufficient number of iterations in modeling the random displacements, or even to numerical errors in the simulation as meshing schemes for pillars with different heights can be different and therefore producing slightly inconsistent results. Nevertheless, putting all the results together, one can conclude that there is a strong correlation between the height of pillars and their corresponding PnBG resistance to change in presence of lattice perturbation.

III. Conclusion

The complete phononic band gap of a phononic crystal (PnC) slab structure made of single solids (in this case single crystal silicon) with embedded air/vacuum holes is utilized to realize PnC-based micromechanical (MM) resonators with higher Qs compared to the conventional MM resonators. We showed that these structures can be integrated with the conventional micromechanical (MM) systems using a CMOS compatible fabrication process and that they can suppress the support loss (an important source of loss in MM resonators) in MM structures. A conventional piezoelectric-on-Si MM resonator and a PnC resonator of the same type are designed, fabricated, tested, and compared to investigate the effect of the support loss and suppressing it in MM resonators.

We showed that by using phononic crystal waveguides, support loss-free mirco/nano-mechanical resonators with large spurious free spectral ranges could be obtained. This solves the problem of the presence of spurious modes in the previously reported micro/nano-mechanical

resonators with support-loss suppression. Although the reported waveguide-based resonator is applied to piezoelectrically-excited resonators, the use of phononic crystal structures to obtain support loss-free resonators can be applied to other resonators with different mechanisms of interrogation.

We have also studied the possibility of forming a new phononic crystal waveguide that can be used as an acoustic filter device. The filter is based on the confinement and guiding the acoustic energy in phononic crystal slab. The structures are made by etching a honeycomb array of holes in a free standing slab. This phononic slab structure exhibit an absolute phononic band gap for all polarization of guided waves inside the slab. A line defect is introduced which allow to confine spatially the acoustic energy and to achieve an acoustic resonator.

We have also shown that the PnCs formed by a Si plate with W pillars could exhibit multiple PnBGs for different lattice symmetries. By accurately designing the geometrical parameters, one can achieve PnBGs in the GHz range that can be easily fabricated for wireless applications. Also, we have shown that the center frequency of these PnBGs can be adjusted by controlling the height of the pillars without changing the lattice spacing. We have additionally shown that the triangular lattice can support a larger number of PnBGs with higher gap to mid-gap ratios compared to the square and honeycomb lattices.

IV. References

1. S. MOHAMMADI, S., EFTEKHAR, A. A., HUNT, W. D., and ADIBI, A.: 'Demonstration of large complete phononic band gaps and waveguiding in high-frequency silicon phononic crystal slabs', in Proc. of 2008 IEEE International Frequency Control Symposium, 19-21 May 2008, pp. 768-772.

2. Van Dyke, K.S.: 'The piezo-electric resonator and its equivalent network by K. S. Van Dyke', *Proceedings of the RIE*, 1928.

3. MOHAMMADI, S., EFTEKHAR, A. A., KHELIF, A. and ADIBI, A.: 'Support loss suppression in micromechanical resonators by the use of phononic band gap structures', in Proc. of 2010 SPIE Photonics West, p. 76090W.

4. SIGALAS, M. M., and ECONOMOU, E. N.: 'Elastic and acoustic wave band structure', J. Sound and Vibration, 1992, 158(2), pp. 377–382

5. BENCHABANE, S., KHELIF, A., RAUCH, J.-Y., ROBERT, L. and LAUDE, V.: 'Evidence for complete surface wave band gap in a piezoelectric phononic crystal', Phys. Rev. E, 2006, 73, 065601(R)

6. KHELIF, A., AOUBIZA, B., MOHAMMADI, S., ADIBI, A. and LAUDE, V.: 'Complete band gaps in two-dimensional phononic crystal slabs', Phys. Rev. E, 2006, 74, 046610

7. MOHAMMADI, S., EFTEKHAR, A. A., KHELIF, A., HUNT, W. D. and ADIBI, A.: 'Evidence of large high frequency complete phononic band gaps in silicon phononic crystal plates', Appl. Phys. Lett., 2008, 92, 221905

8. WU, T.-T., HUANG, Z.-G., TSAI, T.-C. and WU, T.-C.: ‘Evidence of complete band gap and resonances in a plate with periodic stubbed surface’, Appl. Phys. Lett., 2008, 93, 111902

9. PENNEC, Y., DJAFARI-ROUHANI, B., LARABI, H., AKJOUJ, A., GILLET, J. N., VASSEUR, J. O. and THABET, G.: ‘Phonon transport and waveguiding in a phononic crystal made up of cylindrical dots on a thin homogeneous plate’, Phys. Rev. B, 2009, 80, 144302